Modeling and Characterization of CMOS-Fabricated Capacitive Micromachined Ultrasound Transducers

Christopher B. Doody, *Member, IEEE*, *Member, ASME*, Xiaoyang Cheng, *Member, IEEE*, Collin A. Rich, *Member, IEEE*, David F. Lemmerhirt, *Member, IEEE*, and Robert D. White, *Member, IEEE*, *Member, ASME*

***Abstract*—This paper describes the fabrication, characterization, and modeling of complementary metal–oxide–semiconductor (CMOS)-compatible capacitive micromachined ultrasound transducers (CMUTs). The transducers are fabricated using the interconnect and dielectric layers from a standard CMOS fabrication process. Unlike previous efforts toward integrating CMUTs with CMOS electronics, this process adds no microelectromechanical systems-related steps to the CMOS process and requires no critical lithography steps after the CMOS process is complete. Efficient computational models of the transducers were produced through the combined use of finite-element analysis and lumped-element modeling. A method for improved computation of the electrostatic coupling and environmental loading is presented without the need for multiple finite-element computations. Through the use of laser Doppler velocimetry, transient impulse response and steady-state frequency sweep tests were performed. These measurements are compared to the results predicted by the models. The performance characteristics were compared experimentally through changes in the applied bias voltage, device diameter, and medium properties (air, vacuum, oil, and water). Sparse clusters of up to 33 elements were tested in transmit mode in a water tank, achieving a center frequency of 3.5 MHz, a fractional bandwidth of 32%–44%, and pressure amplitudes of 181–184 dB re 1 $\mu\mathrm{Pa}_{\mathrm{rms}}$ at 15 mm from the transducer on axis. [2009-0230]**

***Index Terms*—Acoustic models, acoustic transducers, capacitive micromachined ultrasound transducers (CMUTs), finite-element analysis (FEA), lumped-element modeling, ultrasound.**

I. Introduction

DIAGNOSTIC medical ultrasound requires arrays of ultrasound transducers to transmit acoustic energy into the body and to receive echo information for imaging. Piezoelectric crystals or piezocomposites are utilized for most existing commercial ultrasound technology [1], [2]. Due to the fact that piezoelectric transducers have an acoustic impedance of the same order of magnitude as that of many stiff solids, piezoelectric transducers are an ideal choice for performing ultrasonic investigations directly on solids for applications such as nondestructive evaluation. However, when the objective is to excite and detect ultrasound in human or animal tissue, which has acoustic properties more similar to water than rigid solids, the impedance mismatch between piezoelectrics and tissue results in energy loss [3], [4].

In the case of tissue- or fluid-coupled applications, matching layers are usually placed between the piezoelectric transducer and the medium [3]. However, this solution introduces its own set of problems. Often, materials with the necessary characteristic impedance are hard to find or nonexistent, resulting in the common use of nonoptimal matching layers. In addition, high-frequency transducers require impractically thin matching layers for optimal effect [5].

Recently, capacitive micromachined ultrasound transducers (CMUTs) have been developed as an alternative to piezoelectric transducers [5]–[14]. CMUTs have become a competing microelectromechanical systems (MEMS) technology due to their ability to overcome some of the drawbacks of piezoelectric transducers. Because the structure of a CMUT consists of a flexible thin-film membrane, the device structure is inherently better acoustically matched to tissue compared to rigid piezoelectric crystals. Also, CMUTs exhibit some attractive features such as the possibility of integrating signal processing, signal routing, and power electronics on a chip with the transducers and the possibility of increased bandwidth, which impacts axial resolution [15].

The design of capacitive acoustic transducers for transmit and receive operations in air can be traced back at least to the early part of the 20th century (e.g., [16] and [17]). The earliest example of the use of an electrostatic transducer in submerged operation is by Cantrell *et al.* in the late 1970s [18], [19]. Modern micromachining methods were first applied to electrostatic in-air microphone design by Hohm and Hess in 1989, soon followed by the demonstration of surface-micromachined CMUTs in air by Haller and Khuri-Yakub in 1994 [6], [8] and for submerged operation by Ladabaum *et al.* and Soh *et al.* in 1996 [5], [9].

Researchers have described a variety of CMUT designs and computational models. Both lumped-element modeling and finite-element analysis (FEA) have been employed in the past (e.g., [20] and [21]). Measurements of the device response often include transmit and receive frequency response measurements in a water or oil tank and also the device input electrical impedance (e.g., [5] and [10]). Laser interferometry has also

Manuscript received September 21, 2009; revised October 12, 2010; accepted October 23, 2010. Date of publication December 20, 2010; date of current version February 2, 2011. This work was supported in part by the National Science Foundation under Grant IIP-0450493 and in part by the Michigan Economic Development Corporation. Subject Editor D. L. DeVoe.

C. B. Doody was with Tufts University, Medford, MA 02155 USA. He is now with STD Med, Inc., Stoughton, MA 02072 USA (e-mail: chris.b.doody@gmail.com).

X. Cheng, C. A. Rich, and D. F. Lemmerhirt are with Sonetics Ultrasound, Ann Arbor, MI 48103 USA (e-mail: xcheng@soneticsultrasound.com; crich@soneticsultrasound.com; dlemmerh@soneticsultrasound.com).

R. D. White is with the Mechanical Engineering Department, Tufts University, Medford, MA 02155 USA (e-mail: r.white@tufts.edu).

Color versions of one or more of the figures in this paper are available online at http://ieeexplore.ieee.org.

Digital Object Identifier 10.1109/JMEMS.2010.2093559

been used in the past to characterize CMUT dynamics [22]. These techniques have been applied to a variety of transducer structures, typically achieved using a surface-micromachined MEMS process (e.g., [5]) or a wafer-bonding process (e.g., [23] and [24]).

This paper extends the computational and experimental techniques to CMUT devices fabricated using the layers of a standard n-well complementary metal–oxide–semiconductor (CMOS) circuit fabrication process. This approach offers cost and reliability advantages since an existing commercial integrated-circuit foundry process is used rather than a custom MEMS process. Using a CMOS process also allows seamless integration of front-end readout circuits immediately adjacent to the CMUT devices on the same chip. This approach makes feasible large-scale fully populated 2-D ultrasound arrays, since on-chip multiplexers and low-noise amplifiers help overcome the practical challenges of carrying and conditioning output signals from thousands of transducer elements.

This paper presents modeling and characterization work that supports the development of CMOS-fabricated CMUT elements for large-scale planar ultrasound arrays. The experimental operation of transducer elements and sparse arrays is also presented, demonstrating that CMOS layers can be successfully used to produce high-performance CMUT transducers. This lays the groundwork for the production of densely packed CMUT-in-CMOS systems in the future. Because element mechanics and readout electronics are tightly integrated in these arrays, the modeling efforts have been tailored to support a system-level design approach. After introducing the design and fabrication process for the elements, the hybrid finite-element/lumped-element modeling scheme is presented. This scheme is employed to predict the behavior of various element designs. Laser Doppler velocimetry (LDV), along with water-tank measurements, is used to evaluate the element performance, and these results are compared to the modeling predictions.

II. Design and Fabrication

A. CMUT-in-CMOS Integration Approach

A CMUT device consists of a diaphragm backed with a vacuum cavity and supported by a rigid substrate. Upper and lower conductive electrodes are incorporated into the diaphragm and the substrate, providing the means to electrostatically drive the diaphragm and measure its deflection in response to impinging acoustic pressure. CMUT elements are most typically fabricated using a surface-micromachined fabrication process to create a dielectric or polysilicon membrane by removing an underlying region of sacrificial material [6], [8], [10], [12], [23]. More recently, wafer-bonding processes have been used to create CMUTs with single-crystal silicon membranes [23], [24], including, in recent years, the demonstration of a method of trench isolation that reduces acoustic coupling between elements [25], [26].

To realize the distinct benefits of integrating CMUTs with CMOS circuits, several integration approaches have been used. One method uses flip-chip bonding to attach a readout circuit chip to a CMUT array. Through-wafer vias [27] or trench-isolated through-wafer interconnects [25], [26] are used to carry signals from the device side of the wafer to bonding pads on the back side of the wafer. For reduced complexity, another method uses low-temperature deposition and patterning techniques to create CMUT devices on top of CMOS readout circuits [28], [29]. A third approach, with some similarities to the process presented here, creates CMUT structures using the layers of the CMOS fabrication process itself, with minor MEMS-related alterations to the standard integrated-circuit process flow [7].

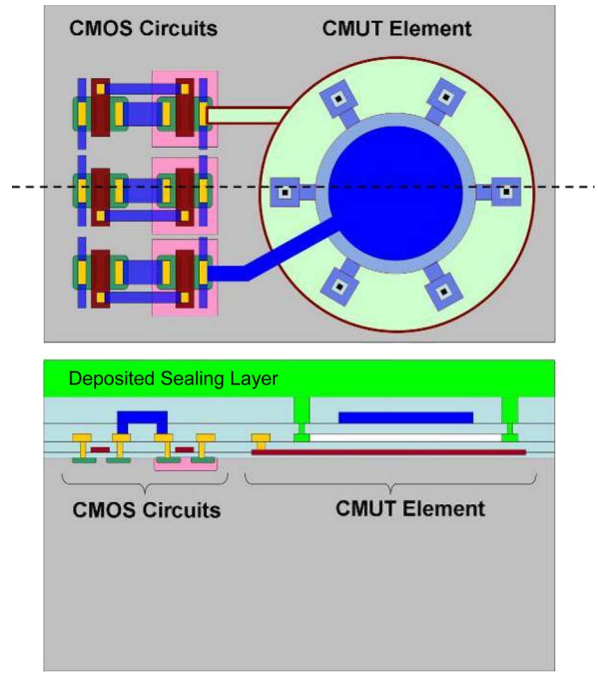

Fig. 1. (Top) Top view of CMUT side by side with CMOS circuits. (Bottom) Cross-sectional view.

The devices presented in this paper are realized using an approach designated as *CMUT-in-CMOS*. The CMUT-in-CMOS process creates the transducer structures using electronic device and interconnect layers which are integral to the CMOS fabrication process. Unlike previous efforts toward integrating CMUTs with electronics, this process adds no MEMS-related steps to the CMOS process and requires no critical lithography steps after the CMOS process is complete. Fig. 1 shows a top view and a cross-sectional illustration indicating the shared CMOS and CMUT layers.

B. Fabrication Process

The CMUT-in-CMOS process begins with a standard foundry CMOS fabrication run, which creates the primary structural layers for the CMUT as well as CMOS transistors on the same chip. For the devices presented here, a 1.5-μm n-well CMOS process with two metal and two polysilicon layers was used (ABN mixed-mode CMOS from On Semiconductor, Phoenix, AZ; accessed through the MOSIS Service, Marina Del Ray, CA). As shown in Figs. 1 and 2, the CMUT devices are formed by defining sacrificial layers, electrodes, and passivation layers within the interconnect metallization and dielectric passivation layers of the CMOS process. In this case, the upper CMOS metallization layer (M2) was used for the top CMUT

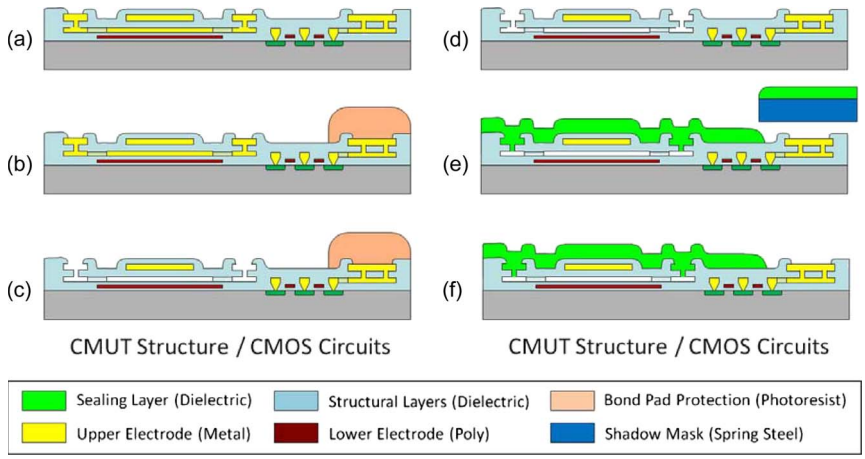

Fig. 2. Illustration of CMUT-in-CMOS fabrication process flow. (a) Silicon die with layers patterned in CMOS foundry process. (b) Photoresist is manually applied (or screen printed) around perimeter to protect bonding pads. (c) CMUT gap is formed by sacrificial wet etching of lower metal layer. (d) Photoresist is stripped; chip is soaked in acetone/methanol and allowed to air dry. (e) Dielectric is deposited to seal the CMUT cavity, and bonding pads are shadow masked to prevent coverage. (f) Completed device is ready for packaging.

TABLE I
MATERIAL PROPERTIES AND LAYER THICKNESSES USED IN THE COMPUTATIONAL MODEL

Layer	Material	Young's Modulus (GPa)	Poisson's ratio	Density (kg/m^3)	Layer Thickness (nm)
	Bulk Silicon	190	0.23	2330	
1	Field Oxide	63.5	0.20	2200	830
2	Doped Polysilicon	172.3	0.23	2330	310
3	Poly-metal Dielectric	74.6	0.20	2200	750
4	Air gap				630
5	Inter-metal dielectric	74.6	0.20	2200	920
6	Aluminum	71.8	0.33	2700	1060
7	Overglass	54.2	0.20	2250	490
8	Nitride Cap	172.5	0.31	3100	690
9	PECVD Silicon OxyNitride	60	0.20	2600	2900

electrode, the lower metal layer (M1) formed the sacrificial layer for the gap, and a polysilicon layer (poly 1) was patterned for the bottom electrode. The silicon dioxide layers over poly 1 and between M1 and M2 provided isolation between the electrodes, and the CMUT membrane was formed by the intermetal dielectric combined with the overglass layer. Typical properties for these layers are given in Table I [32]–[36].

The geometry of the CMUT structure requires violation of several noncritical design rules. Most notably, the overglass openings in the etch-port regions around the CMUT perimeter are smaller than what is recommended. Typical integrated-circuit designs would have overglass openings larger than $50\ \mu\text{m} \times 50\ \mu\text{m}$, since these are used primarily for electrical access to the bonding pads around the chip perimeter and, occasionally, for probe points within its central region. For the CMUT etch ports, $10\ \mu\text{m} \times 10\ \mu\text{m}$ openings were used to avoid consuming an excessive area. Also, typical CMUT designs require curved geometry on the metal and polysilicon layers. These design rule exceptions do not compromise the integrity of the CMOS process, and CMUT chips have been successfully fabricated on shared multiproject wafers without a negative impact.

After the completion of the foundry CMOS process, several straightforward release and sealing steps are performed at the die level. This fabrication sequence is shown in Fig. 2. First, a protective photoresist layer is applied to the bonding pads around the perimeter of the chip. This resist can be manually applied or screen printed. Dimensions and alignment to the underlying features are noncritical, so photolithography is not required. The chip is then immersed in an aggressive aluminum etch solution such as Transene Aluminum Etchant Type A at 70 °C to remove the sacrificial material defining the CMUT gaps. Rinsing is performed in deionized water, acetone, and methanol, and the chip is allowed to dry at room temperature or in a 100 °C oven. Since the device gap is relatively large ($0.6\ \mu\text{m}$), problems with stiction between the membrane and the substrate do not occur. The final fabrication step is the vacuum deposition of the sealing material, typically plasma-enhanced chemical vapor deposition (PECVD) dielectrics and/or Parylene C. This step seals the CMUT cavities by blocking the etch ports and provides surface protection for the chip. For PECVD, shadow masking is used to prevent the perimeter bonding pads from being covered with the dielectric. For Parylene-C coating, the chip can be mounted and wire bonded prior to sealing, so that Parylene can be blanket deposited over the entire device without masking.

Several criteria are used to select the appropriate sealing material and deposition procedure. The deposition temperature must be below 450 °C to avoid damaging the CMOS layers. Mechanical properties such as Young's modulus and residual

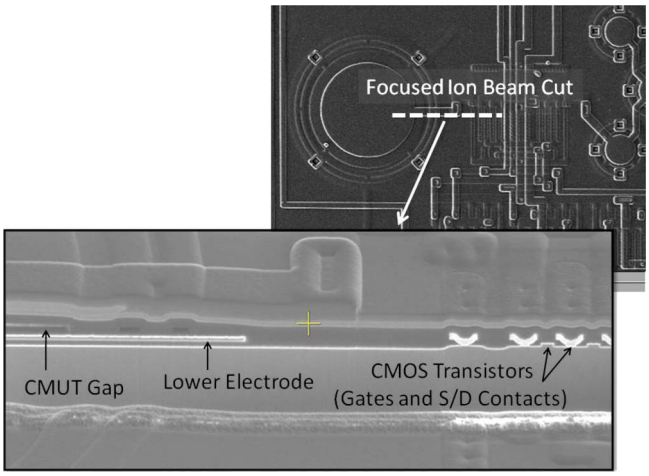

Fig. 3. (Lower) FIB image of CMUT-in-CMOS device cross section. The CMUT gap and lower polysilicon electrode are visible at the left, and the gates and source/drain contacts for the CMOS transistors can be seen at the right. (Upper) Top view of CMUT and on-chip circuits, showing region where FIB cut was made. Cut is approximately 100 μm long.

stress impact the rigidity of the membrane as well as its initial deflection. The sticking coefficient of the material should also be considered, since this determines the thickness needed to close off the etch-port openings and impacts how much deposition will occur within the gap. Parylene C is an attractive sealing material, due to its very low Young's modulus and room-temperature deposition, and it has been used with some success. However, because it has a very low sticking coefficient, Parylene is deposited within the gap, and experiments have revealed deleterious parasitic charging effects which interfere with dc biasing the CMUT during receive operation. Therefore, additional experiments were performed with PECVD silicon dioxide, silicon nitride, and silicon oxynitride, deposited at 380 °C–400 °C. Favorable results without substantial charging effects were obtained with these PECVD materials. The results given in this paper use 3 μm of PECVD oxynitride, which has been tuned to provide lower residual stress compared to PECVD nitride or oxide [36].

The CMUT-in-CMOS approach has been successfully demonstrated, both for the devices presented here and for larger imaging arrays with on-chip receive circuitry [37]. Fig. 3 shows a focused ion beam (FIB) image of a released and sealed device, together with a cross-sectional view showing CMUT features (gap and lower electrode) alongside CMOS circuit components (polysilicon gates and metal source/drain contacts). The fabrication process provides advantages in terms of simplicity, cost, yield, and repeatability. All of the critical lithography steps and thin-film deposition steps for the CMUT structures occur during the CMOS foundry process, which is a tightly controlled high-volume manufacturing process that benefits from the semiconductor industry's huge investment in infrastructure and engineering for integrated-circuit production. The steps after the foundry CMOS process are straightforward and low cost (wet etching without critical timing and blanket deposition of low-temperature dielectrics, which can occur in relatively affordable PECVD and Parylene C deposition chambers). As compared to other CMUT fabrication approaches, the CMUT-in-CMOS process is likely to produce higher yield chips at a lower cost, since few custom low-volume process steps are needed. It should be noted, however, that the fundamental sensitivity of the CMUT-in-CMOS transducer structures themselves may be limited compared to custom approaches, since the layer thicknesses (notably the sacrificial layer and the diaphragm thickness) are predetermined by the CMOS process selected. On the other hand, because CMOS circuitry can be integrated so tightly with the CMUTs at no additional cost or fabrication effort, there is room for significant circuit-based signal-to-noise improvements (e.g., low-noise amplifiers, time-gain control circuits, and, perhaps, analog-to-digital converters can be included on a chip, minimizing parasitics and system-level noise contributions). The modeling work presented in this paper contributes to ongoing efforts to evaluate the overall benefits and limitations of the CMUT-in-CMOS approach, providing an important computational tool to explore transducer/circuit/system design and performance tradeoffs.

C. Device Design

The CMUT-in-CMOS integration approach requires the design of the CMUT structure to be constrained to the layers available within the integrated-circuit manufacturing process. The CMUT membrane diameter and thickness are designed to achieve a desired resonant frequency, which is targeted to meet the demands of a particular imaging application (e.g., higher frequencies yield better lateral and axial resolution, while lower frequencies allow greater penetration depth). The CMUTs presented here are designed for the 1–5-MHz range typically used for abdominal ultrasound imaging.

The center frequency of a circular membrane scales with both the thickness and diameter of the membrane. Since the lateral dimensions of the CMUT are defined photolithographically, a range of diameters is achievable. The membrane thickness is constrained by the layer thicknesses available within the fabrication technology. Thinner membranes provide increased mechanical sensitivity due to the increased volume compliance, resulting in larger capacitance changes for a given applied pressure. Thicker membranes decrease the volume compliance, allowing higher applied bias voltages prior to pull-in or collapse.

The layer combinations available within the chosen CMOS process dictate that the CMUT membrane will be at least 2.0 μm thick, with a more typical thickness of 3.0–7.0 μm, depending on the thickness of the post-CMOS sealing layer. To obtain a center frequency between 1.0 and 5.0 MHz for abdominal imaging, with a structure constructed mainly of silicon dioxide and aluminum and mass loaded by a waterlike fluid environment, a CMUT diameter of 100 μm was chosen. Devices with diameters between 30 and 100 μm were designed for evaluation of the frequency response. Models that may be used to make these design choices are described in detail later in this paper.

Fig. 4 shows a photograph of a 100-μm-diameter CMUT prior to release etching. As shown, the device is designed with etch ports offset from the central membrane region. This design feature encourages etch-port sealing with minimal deposition of

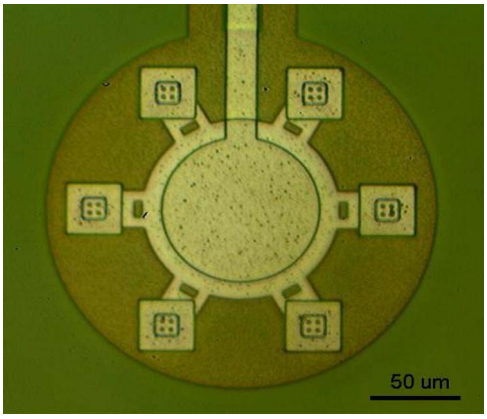

Fig. 4. Photograph of a 100-μm-diameter CMUT showing etch ports offset from device membrane.

the sealing material within the gap. Design variations with etch ports within the membrane region have also been evaluated.

III. Mathematical Modeling

A. Lumped-Element Modeling

Lumped-element acoustic models were used in order to create a dynamic computational model of the transducers. Two coupled electrical-mechanical acoustic models of a single CMUT element are shown in Fig. 5. The left-hand model represents the element in "transmit" mode. In "transmit" mode, the driving RF voltage $V_{\rm ac}$ is applied to the element's diaphragm. The output of the model is the diaphragm's volume velocity $U_{\rm dia}$. The right-hand model represents the element in "receive" mode. In receive mode, an external acoustic pressure $P_{\rm in}$ is applied to the diaphragm face. The result is a volume velocity which is converted to a current by the ideal transformer, feeding from there to the receive electronics.

The lumped-element acoustic model incorporates environmental loading, diaphragm mass, diaphragm acoustic compliance, the negative electrostatic spring, and backing cavity compliance. Some of these elements were calculated analytically using standard expressions [30], [31]. Other elements were determined numerically using finite-element methods as described hereinafter.

Environmental mass loading $Z_{\rm env}$ was computed using a formulation similar to the four components for a rigid baffled piston radiating into an infinite half-space suggested by Beranek [30]

$$\begin{aligned} Z_{\rm env} = {} & [M_{A1}s(R_{A1}+R_{A2}+R_{A1}R_{A2}C_{A1}s)] \\ & \cdot \left[C_{A1}M_{A1}R_{A1}s^2+(M_{A1}+C_{A1}R_{A1}R_{A2})s \right. \\ & \left. +R_{A1}+R_{A2}\right]^{-1} \end{aligned} \tag{1}$$

$$R_{A1} = 0.243\rho c/(\pi a^2) \tag{2}$$

$$R_{A2} = \rho c/(\pi a^2) \tag{3}$$

$$M_{A1} = 0.643\rho/(\pi a) \tag{4}$$

$$C_{A1} = 5.52(\pi a^3)/(\rho c^2) \tag{5}$$

where ρ and c are the density for the environment and the speed of sound, respectively, and s is the Laplace transform variable. In the CMUT, the diaphragm moves as a bending structure, not as a rigid piston. Therefore, the expressions previously presented have the same scaling with the characteristic impedance of the medium (ρc), and the diaphragm radius, as Beranek's result, but the coefficients in front of each term are modified. The coefficients were determined by computing, using FEA, the acoustic field transmitted into an infinite acoustic half-space by an axisymmetric baffled structure oscillating in a simply supported static bending modeshape

$$\psi(r) = 1 - 2\frac{3+\upsilon}{5+\upsilon}\left(\frac{r}{a}\right)^2 + \frac{1+\upsilon}{5+\upsilon}\left(\frac{r}{a}\right)^4. \tag{6}$$

The simply supported static bending modeshape is selected based on electrostatic finite-element models, shown later in this paper, which show this shape to be a good match to the electrostatically excited shape of the transducer deflection. A value of 0.2 is used for ν, as the bending structure is predominantly silicon dioxide and PECVD oxynitride. The acoustic impedance $Z_{\rm env}$ is the ratio of the volume velocity of the transducer to the effective pressure at the surface. In order to conserve transmitted power, the effective pressure is the surface integral of the surface velocity times the local pressure, normalized by the total volume velocity

$$P_{\rm eff} = \frac{1}{U_{\rm dia}}\int_A uPdA. \tag{7}$$

A series of computations was run at various frequencies. A convergence study was conducted to ensure convergence of the computation. The coefficient for M_{A1} determines the low-frequency imaginary asymptote. The coefficient for R_{A2} determines the high-frequency real asymptote. R_{A1} is then determined in combination with R_{A2} and M_{A1} to match the low-frequency real asymptote. Finally, the coefficient for C_{A1}, which has an impact only in the transition region at high ka, was determined in order to minimize the mean square error between the FEA and analytical computations over the range of frequencies between $ka = 0.1$ and $ka = 3.0$. A comparison between the finite-element result and the analytical approximation previously given is shown in Fig. 6. The approximation is good for $ka < 2$.

The final pure acoustic element in the model comes from the small cavity behind the membrane. The cavity is filled with the residual rarefied gas that is left during the low-pressure sealing and passivation process (PECVD or Parylene coating). This cavity acts as a small mechanical spring as it is compressed by the motion of the diaphragm. For CMUTs with a relatively low vacuum within the backing cavity, this gas may not contribute much stiffness but may be easily included. The cavity compliance can be calculated by [31]

$$C_{\rm cav} = V_{\rm cav}/(\rho_{\rm cav}c^2) \tag{8}$$

where $V_{\rm cav}$ is the volume of the cavity, c is the speed of sound in the cavity (for air, this is not strongly affected by pressure), and $\rho_{\rm cav}$ is the density of the rarefied air in the cavity, which may be approximated by the ideal gas law

$$\rho_{\rm cav} = \rho_0\frac{P_{\rm cav}}{P_0} \tag{9}$$

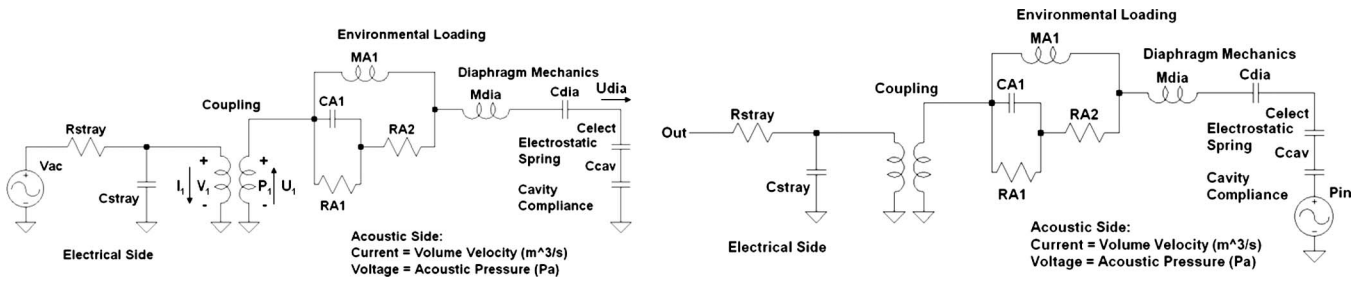

Fig. 5. Lumped-element model of the transducer in (left) transmit mode and (right) receive mode.

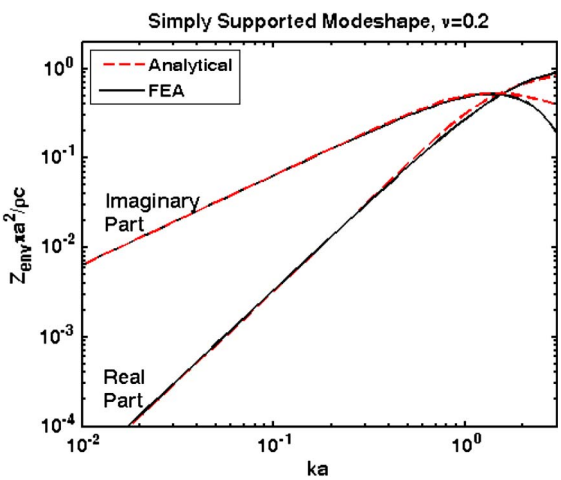

Fig. 6. Comparison of finite-element and analytical approximation to the environmental loading presented in nondimensional form.

where the density in the cavity is the density of air at atmospheric pressure ρ_0 multiplied by the ratio of the cavity pressure to atmospheric pressure. For the devices modeled in this paper, P_{cav} is 300 mT, which is the pressure during the PECVD.

B. Electromechanical Coupling

Electromechanical coupling can be computed by considering the capacitor formed between the aluminum and the doped polysilicon electrodes, along with the two intervening dielectrics and the vacuum gap (see Figs. 1 and 7). In order for energy to be conserved in the coupling, the acoustic power flowing into one port of the transformer must equal the electrical power flowing out of the second port. By carefully considering this conservation, we can determine the electromechanical coupling, including incomplete electrode coverage and a variable height vacuum gap. Consider first the height of the vacuum gap, which, for this axisymmetric design, is a function of radial position

$$g_1 = d_1 - x\Psi(r) \tag{10}$$

where d_1 is the undeflected height of the vacuum gap, $\Psi(r)$ is the radial shape of the static deflection, and x is the magnitude of the static deflection. Note that, at this point, $\Psi(r)$ is an unknown function, and x is an unknown magnitude that will depend on the applied dc bias. Consider now an incremental deflection from this equilibrium position described by an infinitesimal change in x, which is δx. During this deflection, we consider the voltage and electrostatic pressure to be held constant. The incremental change in the energy stored in the capacitor must equal the acoustic energy delivered

$$\begin{aligned} \delta E_{\text{acoustic}} &= P_{\text{elect}} \delta Q \\ \delta E_{\text{elect}} &= \frac{1}{2} V^2 \delta C \end{aligned} \tag{11}$$

where C is the capacitance between the electrodes, V is the applied voltage, P_{elect} is the resulting electrostatic pressure, and δQ is the volume displacement. We now make use of the equivalent capacitance for the series capacitance across multiple dielectric layers

$$C = \int_{A_1} \left(\frac{d_1 - x\Psi(r)}{\varepsilon_1} + \frac{d_2}{\varepsilon_2} + \frac{d_3}{\varepsilon_3} \right)^{-1} dA \tag{12}$$

where ε_1 is the dielectric constant for the vacuum gap, d_2, d_3, ε_2, and ε_3 are the thicknesses and dielectric constants for the other dielectric layers, and the integral is over the area of the smaller electrode. The incremental change in capacitance is then

$$\begin{aligned} \delta C &= \frac{\partial C}{\partial x} \delta x \\ &= \int_{A_1} - \left(\frac{d_1 - x\Psi(r)}{\varepsilon_1} + \frac{d_2}{\varepsilon_2} + \frac{d_3}{\varepsilon_3} \right)^{-2} \left(\frac{-\Psi(r)}{\varepsilon_1} \right) dA. \end{aligned} \tag{13}$$

The increment in volume displacement used in (11) comes directly from the area integral of displacement

$$\delta Q = \int_{A_2} \delta x \Psi(r) dA \tag{14}$$

where, here, the integral is over the entire deflecting diaphragm area A_2. If the two energy increments from (11) are equated,

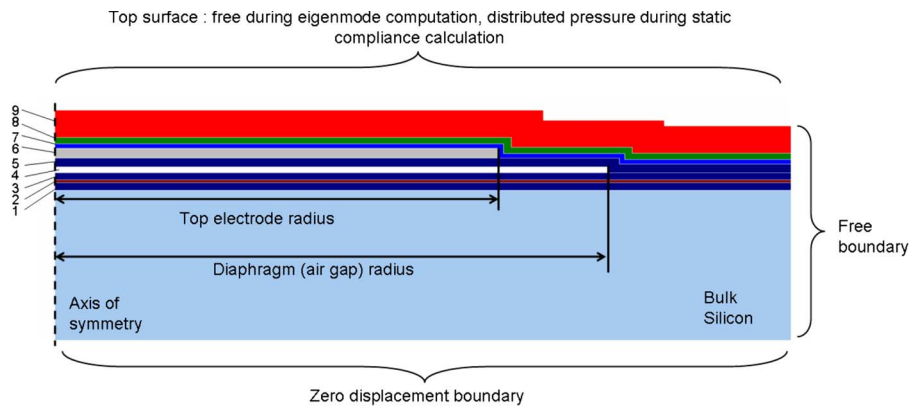

Fig. 7. Axisymmetric cross section of the transducer.

we can solve for the equivalent electrostatic pressure

$$P_{\text{elect}} = \frac{1}{2\varepsilon_1} V^2 \cdot \frac{\int_{A_1} \Psi(r) \left(\frac{d_1 - x\Psi(r)}{\varepsilon_1} + \frac{d_2}{\varepsilon_2} + \frac{d_3}{\varepsilon_3} \right)^{-2} dA}{\int_{A_2} \Psi(r) dA}. \tag{15}$$

In the case of a dc bias summed with a pure tone ac voltage

$$\begin{aligned} V &= V_{\text{bias}} + V_{\text{ac}} \cos(\omega t) \\ V^2 &= V_{\text{bias}}^2 + \frac{1}{2} V_{\text{ac}}^2 \ldots \\ &\quad + 2V_{\text{ac}} V_{\text{bias}} \cos(\omega t) + \frac{1}{2} V_{\text{ac}}^2 \cos(2\omega t). \end{aligned} \tag{16}$$

If we are concerned only with the linear response (the response at the drive frequency ω), then the linear coupling constant for the ideal transformer is

$$\begin{aligned} N &= \frac{P_{\text{elect}}}{V_{\text{ac}}} \\ &= \left(\frac{V_{\text{bias}}}{\varepsilon_1} \right) \cdot \frac{\int_{A_1} \Psi(r) \left(\frac{d_1 - x\Psi(r)}{\varepsilon_1} + \frac{d_2}{\varepsilon_2} + \frac{d_3}{\varepsilon_3} \right)^{-2} dA}{\int_{A_2} \Psi(r) dA}. \end{aligned} \tag{17}$$

Note that N has units of Pa/V or, equivalently, A/(m/s) (in SI units). It is a bidirectional coupling constant for the ideal transformer. $d_1 - x\Psi(r)$ is the vacuum gap computed with the dc bias applied. For a dc bias well below the pull-in voltage, $x\Psi(r)$ is much smaller than d_1, and we can approximate N as

$$N \approx \left(\frac{V_{\text{bias}}}{\varepsilon_1} \right) \cdot \left(\frac{d_1}{\varepsilon_1} + \frac{d_2}{\varepsilon_2} + \frac{d_3}{\varepsilon_3} \right)^{-2} \frac{\int_{A_1} \Psi(r) dA}{\int_{A_2} \Psi(r) dA}. \tag{18}$$

Note that, for incomplete electrode coverage, the ratio of the area integrals of the static deflection modeshapes in (18) must still be computed even for low dc biases. For larger bias voltages, $x\Psi(r)$ cannot be neglected with respect to d_1 and must be determined by a static structural analysis, as described hereinafter in the discussion of finite-element computations.

The electrostatic spring compliance C_{elect} can also be determined from a similar analysis. Returning to (15), the linear electrostatic spring compliance comes from the change in electrostatic pressure δP due to a small change in volume displacement δQ with only a dc bias applied

$$\begin{aligned} C_{\text{elect}} &= -\left(\frac{\partial P_{\text{elect}}}{\partial Q} \right)^{-1} \\ &= -\left(\frac{\partial P_{\text{elect}}}{\partial x} \frac{\partial x}{\partial Q} \right)^{-1} \\ &= \left(\frac{-\varepsilon_1^2}{V_{\text{bias}}^2} \right) \times \frac{\left(\int_{A_2} \Psi(r) dA \right)^2}{\int_{A_1} \Psi^2(r) \left(\frac{d_1 - x\Psi(r)}{\varepsilon_1} + \frac{d_2}{\varepsilon_2} + \frac{d_3}{\varepsilon_3} \right)^{-3} dA}. \end{aligned} \tag{19}$$

It is important to note that C_{elect} should have a negative value. Once again, we need to determine $\Psi(r)$ and x before C_{elect} can be computed. At bias voltages well below the pull-in voltage of the transducer, the change in the vacuum gap can be neglected, and we can approximate C_{elect} as

$$C_{\text{elect}} \approx \left(\frac{-\varepsilon_1^2}{V_{\text{bias}}^2} \right) \left(\frac{d_1}{\varepsilon_1} + \frac{d_2}{\varepsilon_2} + \frac{d_3}{\varepsilon_3} \right)^3 \frac{\left(\int_{A_2} \Psi(r) dA \right)^2}{\int_{A_1} \Psi^2(r) dA}. \tag{20}$$

C. Pure AC Drive

Although all of the results presented in this paper use a dc bias plus pure tone ac to drive the CMUT, a brief note regarding the pure ac drive is needed. Returning to the voltage expression shown in (16), if the dc bias is zero, there are no terms remaining at ω. Thus, with the pure ac drive, we expect instead to see a mechanical response primarily at twice the drive frequency 2ω. The model as presented can be used for this case with a few simple modifications. Referring to (16), we see that, in (17)–(20), V_{bias} should be replaced with $V_{\text{ac}}/4$. Finally, when computing $x\Psi(r)$ using static FEA, the static driving voltage is $V_{\text{ac}}^2/2$ rather than V_{bias}^2. The model in Fig. 5 can now be applied, with the driving voltage of magnitude V_{ac} at a frequency of 2ω. The results on the acoustic side (volume velocities and pressures) will correctly capture the response.

D. FEA

Due to the complex cross-sectional geometry of the transducer designs, FEA was used to determine the diaphragm compliance C_{dia}, effective diaphragm mass M_{dia}, and the static deflection in response to the applied dc bias $x\Psi(r)$, which, in turn, affects the electromechanical coupling coefficient N and the electrostatic spring C_{elect} as previously described.

COMSOL Multiphysics was used to model the complex geometry of each transducer as an axisymmetric cross section. Linear elastic materials were used. Triangular Lagrange elements with quadratic-shaped functions were employed to mesh the structure. A convergence study was conducted to ensure that the solution was fully converged. Six thousand two hundred elements were sufficient for convergence to better than 0.5%. The element mesh was dense within the thin bending layers and coarse in the region of the bulk silicon far from the active portions of the model. Within the thin layers, the element size is on the order of 0.5 μm, with at least two elements through the thickness of each layer. The element size becomes coarser gradually through the silicon base toward the bottom of the model, reaching a maximum element size of approximately 5 μm.

A layout of the transducer's cross section, along with the boundary conditions used in the simulation, is shown in Fig. 7. The transducer is composed of a bulk silicon base, several thin-film dielectric and metal layers, and a passivation layer. There is an "air gap" (filled with rarefied gas) in between the moving diaphragm and the base layers. In the FEA model, this is treated as a vacuum gap for the purposes of the computation. Two conductive layers (aluminum and doped polysilicon) form the variable parallel-plate capacitor for electrical-mechanical coupling.

The thicknesses for each of the layers in the CMOS process are taken from the careful work of Marshall and Vernier [32]. The elastic modulus and density for each of the CMOS layers are taken from the work of Marshall *et al.* [33]. The Poisson ratio of the layers is taken from textbook values for the various materials [34]. The PECVD oxynitride sealing layer is the layer for which we have the least characterization data. Here, we take the density and Poisson ratio from textbooks [34], [35] and the elastic modulus from the average values determined by Thurn *et al.* in their study of the unannealed mechanical properties of PECVD oxynitride films [36]. The values are summarized in Table I. It should be noted that the modulus of the PECVD films can vary widely; this is expected to be the single most variable parameter in the process. Variations in this modulus will change the value of the diaphragm compliance C_{dia}, resulting mainly in shifts of the resonant frequency.

C_{dia}, representing the *in vacuo* diaphragm acoustic compliance, was calculated by applying a unit uniform pressure load to the top surface and computing the resulting static deflection. The acoustic compliance is the surface integral of the displacement divided by the magnitude of the applied pressure.

An *in vacuo* eigenfrequency analysis was then performed on the same model in order to determine the diaphragm effective mass M_{dia} according to

$$\frac{1}{\sqrt{M_{\mathrm{dia}} \cdot C_{\mathrm{dia}}}} = f1 \cdot 2\pi \tag{21}$$

TABLE II
RESULTS OF THE FINITE-ELEMENT COMPUTATION FOR A 100- AND AN 80-μm-DIAMETER CMUT

	Air Gap Radius (μm)	Electrode Radius (μm)	C_{dia} (m^3/Pa)	f_1 (MHz)	u_{ctr} (m/m^3)
#1	50	40	$3.99 \cdot 10^{-22}$	4.59	$3.08 \cdot 10^{8}$
#2	40	32	$1.23 \cdot 10^{-22}$	6.91	$3.08 \cdot 10^{8}$

where f_1 is the first eigenfrequency in hertz determined from FEA.

For comparison to laser vibrometry (LDV) measurements, it is convenient to know the relationship between the centerpoint displacement (which is measured) and the volume velocity (which we compute). We therefore also extract from FEA the ratio of the static centerpoint displacement to the static volume displacement u_{ctr}. From this, we can easily compute centerpoint displacement u from volume velocity U_{dia}

$$u = \frac{u_{\mathrm{ctr}} U_{\mathrm{dia}}}{j\omega}. \tag{22}$$

The results of the FEA computations are shown in Table II. Finally, we need to determine the modeshape and static deflection due to the applied dc bias $x\Psi(r)$ in order to compute the two electromechanical coupling parameters previously described. An iterative analysis is performed, where the pressure applied to the top electrode is a function of position and deflection

$$P(r) = \frac{1}{2\varepsilon_1} V_{\mathrm{bias}}^2 \cdot \left(\frac{d_1 - x(r)}{\varepsilon_1} + \frac{d_2}{\varepsilon_2} + \frac{d_3}{\varepsilon_3} \right)^{-2}. \tag{23}$$

The deflection $x(r)$ is a result of the linear static analysis, requiring an iterative procedure to be applied in COMSOL to find the converged solution. Once the solution converges for a given V_{bias}, $x(r) = x\Psi(r)$ is known, and we can numerically compute the area integrals in (17) and (19).

Alternatively, the computation can be conducted analytically assuming that $\Psi(r)$ is the axisymmetric static bending modeshape given before in (6). An iterative procedure is then used to compute x. The volume displacement is determined by applying the effective electrostatic pressure to a series combination of the static diaphragm compliance C_{dia} and the electrostatic spring C_{elect}. The deflection amplitude x is the volume displacement divided by the area integral of the modeshape

$$x = \frac{1}{\int_{A_1} \psi(r) dA} \left(\frac{1}{C_{\mathrm{dia}}} + \frac{1}{C_{\mathrm{elect}}} \right)^{-1} \left(\frac{N V_{\mathrm{bias}}}{2} + P_{\mathrm{atm}} \right). \tag{24}$$

The computation begins assuming that x is zero and then iterates on the computation until x converges. The results obtained by this iterative analytical procedure are very similar to the results obtained by FEA, as shown in Figs. 8 and 9. It is for this reason that we use the simply supported modeshape. Since the iterative analytical computation is less computationally expensive than the FEA run, we prefer this method and use the analytical method with the modeshape shown in (6) to produce the results shown in the rest of this paper.

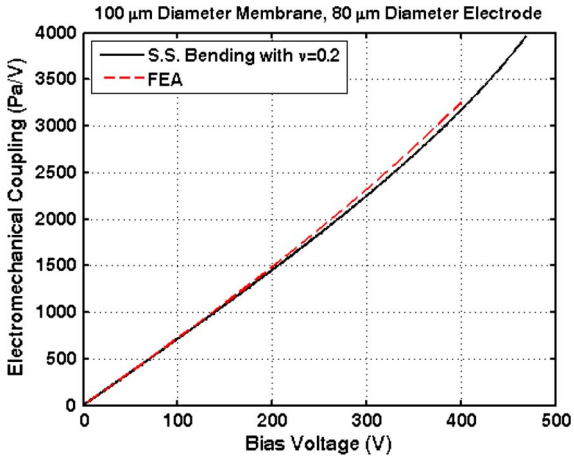

Fig. 8. Comparison of FEA and analytical results for the coupling constant N as a function of applied bias voltage.

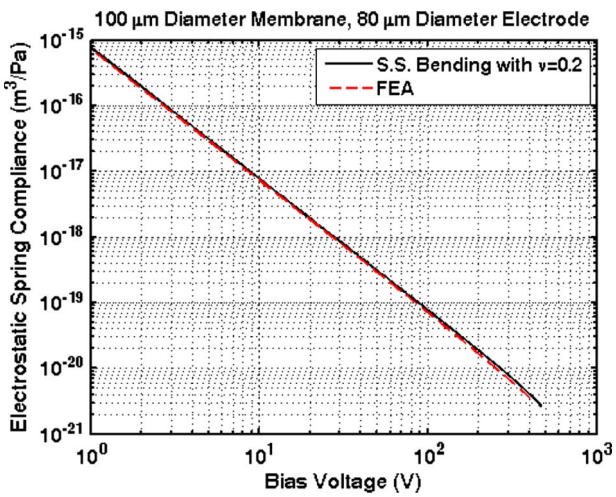

Fig. 9. Comparison of FEA and analytical results for the electrostatic spring magnitude $-C_{\text{elect}}$ as a function of applied bias voltage.

With these parameters in hand, the dynamic model shown in Fig. 5 can be applied to compute the membrane volume velocity or the centerpoint displacement in response to a given dc bias plus RF drive. A sample frequency response plot is shown in Fig. 10 for a 100-μm-diameter CMUT in transmit mode. In air, the primary resonance for this particular device is predicted to be 4.6 MHz, with a very narrow fractional bandwidth of 0.06%. In a water environment, the model predicts a 3.0-MHz center frequency, with a fractional bandwidth of 22% for the same device. The computed fractional bandwidths are based on the volume velocity, as this is the most relevant parameter to source strength.

E. Array Computations

In the results shown hereinafter, both single elements and arrays of elements are discussed. For array testing, the transmitted pressure response is measured on axis. In order to compare the results with model predictions, a simple model of array transmit response is required.

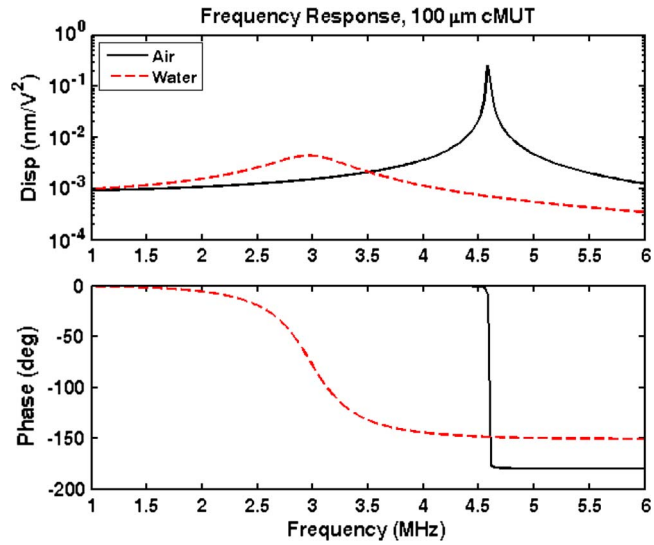

Fig. 10. Modeled transmit frequency response for a single element in air and water environments.

At low frequencies $(ka \ll 1)$, we can treat the element as a baffled simple source, and assuming that we are in the far field and there are no reflections

$$P_m = \frac{j\rho f}{R_m} e^{-jkR_m} U_m \tag{25}$$

where ρ is the density of the environment, f is the frequency of the drive in hertz, R_m is the distance from the mth to the field point, and k is the wavenumber in the environment. As with all previous quantities, the pressure is harmonic at the drive frequency, and we are considering steady-state pressures only. At the frequency of operation (3 MHz in water), for these size elements (50-μm radius), directivity from the finite size of the element results in at most 3% deviation from omnidirectional radiation. This expectation is based on standard baffled piston directionality expressions as supported by finite-element calculations for a simply supported oscillation shape. In addition, water-tank measurements are taken at distances of more than 100 diameters, placing the field point well into the far field. Thus, the monopole radiation assumption is justified. The full far-field pressure can be computed by summing the monopole fields from each element

$$P(x, y, z) = j\rho f \cdot \sum_{m=1}^{N} \frac{1}{R_m} \cdot U_m e^{-jkR_m}. \tag{26}$$

In this computation, coupling between the elements in the array is neglected. This coupling can come from multiple sources, including acoustic coupling through the environment, structural vibrations in the substrate, and electrical coupling between elements. Acoustic coupling in the environment can be included in the calculation and does have an impact on the computed pressure field. However, the uncoupled model presented here matches the experimental results more closely in terms of bandwidth and absolute pressure than a model that includes full acoustic coupling between the elements, suggesting that acoustic coupling is not the dominant coupling mechanism. The other sources of coupling (structural and electrical) are not well

known for this design and, hence, could only be included in an *ad hoc* fashion, which will not be done.

IV. Experimental Results

A. Laser Vibrometry Results

LDV was used to characterize individual element vibration. This was accomplished using a Polytec fiber-optic single-point vibrometer type OFV-551, with an OFV 3001 controller incorporating the OVD-30 high-frequency displacement decoder (Polytec GmbH, Waldbronn, Germany). The decoder has a 50-kHz–20-MHz bandwidth and has been calibrated by Polytec within the last two years. An Agilent 33220A signal generator is used to provide the excitation voltages (Agilent, Santa Clara, CA). A National Instruments high-speed digitizer board type PCI-5124 with a 200-MHz sample rate and 12 b of accuracy was used to capture data in the Labview programming environment (National Instruments, Austin, TX). Frequency sweep tests were performed on CMUT elements of two different diameters (80 and 100 μm) in three environments (vacuum, air, and oil), with a varying dc bias. The data were analyzed using Fourier techniques in software to extract the peak response at the drive frequency and determine the relative phase and magnitude as compared to the excitation signal.

The peak displacement results are reported normalized to the product of the dc bias and the peak ac voltage (in nm/V^2). Velocity can be computed from displacement simply by multiplying by $j\omega$. Fractional bandwidths and peak frequencies are always computed based on velocity, not displacement, as velocity is the most relevant quantity to transmitted pressure. The test results show a peak frequency between 3 and 7.6 MHz, depending on the experimental case in question, with a low-frequency gain on the order of 10^{-3} to 10^{-2} nm/V^2. The fractional bandwidth varies from 0.3% to 23% for single elements, depending mainly on the environment.

The centerpoint displacement calculated from the model was compared to the frequency sweep data obtained from the CMUT elements. A frequency plot comparison for a 100-μm-diameter element tested in air with a 9-V_{dc} bias and 2-V_{pp} ac drive is shown in Fig. 11. The computational model predicted a peak frequency of 4.6 MHz, which is similar to the 5.1-MHz resonant frequency measured experimentally. The slightly higher resonant frequency seen experimentally could be due to material property variations, particularly in the PECVD oxynitride sealing layer, or slightly tensile residual stresses. The measured fractional bandwidth is 0.6%, which is somewhat wider than the predicted 0.06%, suggesting that some unmodeled damping mechanisms are present. Adding as little as 0.5% material damping to the computational model will bring the in-air bandwidth into agreement with the measured result. The model and experimental results agree very well as to the low-frequency amplitude, suggesting that the electrostatic coupling for this case is well captured.

Comparisons between frequency sweeps with different dc biases were also performed on the same 100-μm-diameter element in air. The experimental and computational results for 40- and 80-V_{dc} biases are shown in Figs. 12 and 13. As the dc

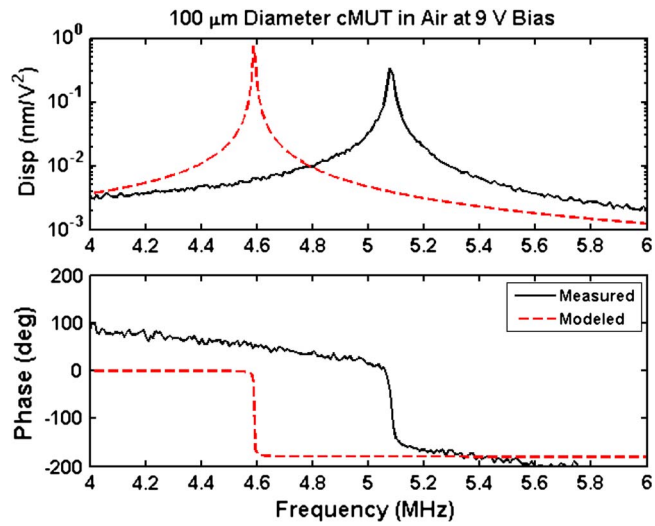

Fig. 11. Frequency response comparison between a computational result and experimental data.

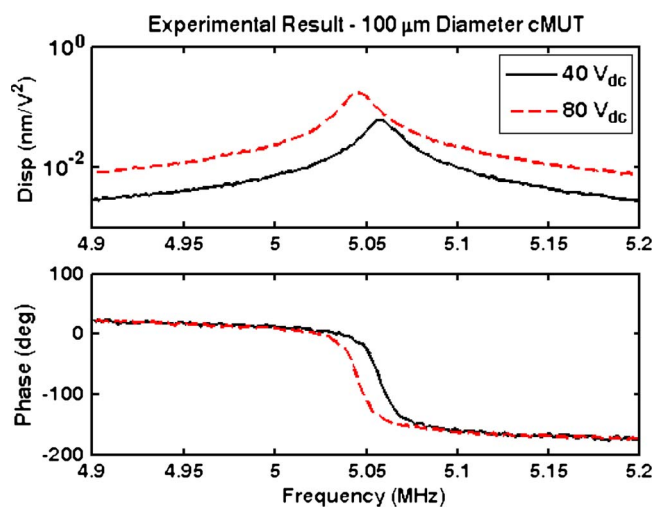

Fig. 12. Experimental frequency response comparison for different dc biases.

bias increases, the resonant frequency decreases slightly, and the peak displacement increases. The reduction in the resonant frequency is due to the increase in the magnitude of the negative electrostatic spring C_{elect} with bias. The increase in magnitude is due to an increase in the coupling constant N which is due to a decrease in the effective gap height d_1. While the model does show both effects, the change in both the peak frequency and the magnitude of the response is greater in the experimental case.

The effect of transducer diameter on the resonant frequency was also tested. A frequency sweep, shown in Fig. 14 for two different biases, was performed on an 80-μm-diameter CMUT. The 80-μm device was from the same chip as the 100-μm device previously shown; thus, all layer thicknesses and materials remained the same. The 80-μm-diameter element shows a higher primary resonance occurring at 7.6 MHz, as well as a smaller fractional bandwidth of 0.24%. This is consistent with the model results, which predict a 6.91-MHz center frequency and 0.04% fractional bandwidth. As with the larger CMUT, the model is predicting a slightly lower resonant frequency than what is measured and a narrower fractional bandwidth. Once

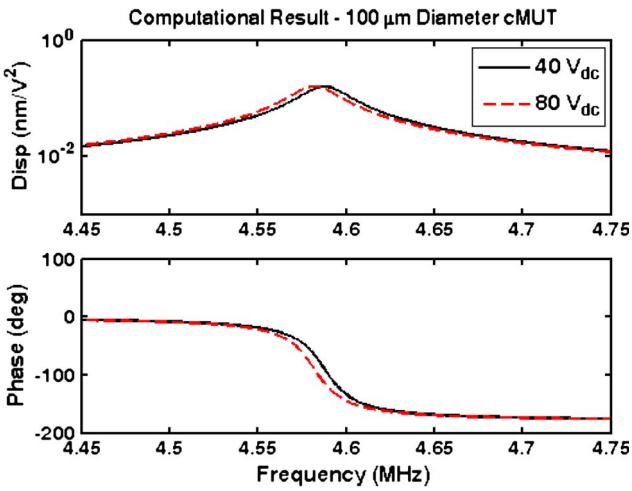

Fig. 13. Computational frequency response comparison for different dc biases.

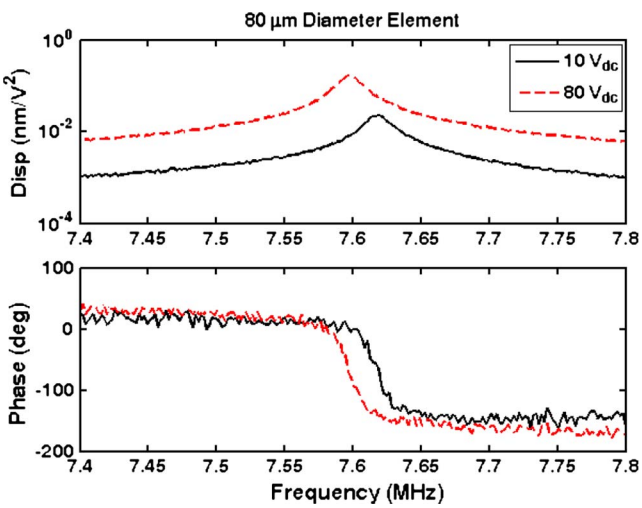

Fig. 14. Experimental frequency response for an 80-μm-diameter element for different dc biases.

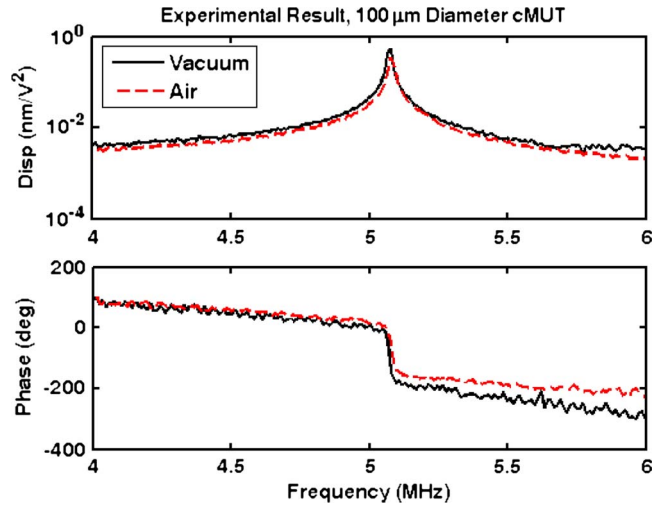

Fig. 15. Frequency response comparison for air versus vacuum.

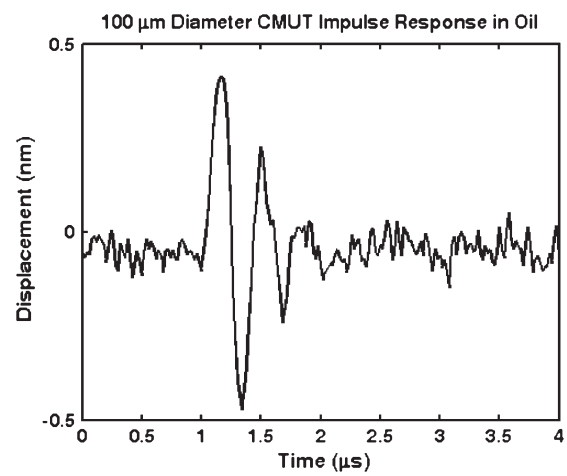

Fig. 16. Transient impulse response of a single 100-μm-diameter element in oil (LDV measurement).

again, this indicates that the PECVD oxynitride modulus may be somewhat higher than what is expected, or some tensile stresses may be present. Again, unmodeled material damping appears to be present.

Frequency sweeps of the transducer were also performed in vacuum. A vacuum chamber was built for testing the transducer at 1.08 torr while maintaining optical access to the diaphragm. A plot comparing the response at atmospheric and low pressure is shown in Fig. 15. In vacuum, the transducer shows an identical result to air, with a peak frequency of 5.8 MHz and a fractional bandwidth of 0.6%. This suggests that the environment is not providing significant damping or mass loading to the device in either air or vacuum; the dynamics are dominated by the structure itself. This is consistent with the modeling results, which show no change in the resonant frequency when moving to a vacuum environment. The modeled fractional bandwidth decreases slightly in vacuum, as losses to the environment are the only damping mechanism in the model. If material damping was included at 0.5% as suggested earlier, the material damping would dominate, and the model would show no change in the fractional bandwidth when moving from air to vacuum, which is consistent with the experimental results.

Finally, the transducer was tested in an oil environment. A drop of 200-cSt silicone oil with a density of 1000 kg/m^3 was applied to the CMUT surface for this test. The speed of sound in silicone oil, which is 1500 m/s, is similar to that in water, but oil is nonconductive, reducing the possibility of short circuits within the test fixture. Both water and oil have similar acoustic properties to tissue and can therefore be used for testing. In oil, the signal-to-noise ratio is lower compared to that in air, and the peak is much suppressed due to damping. We therefore found it more effective to measure a transient impulse response, rather than an ac frequency sweep, to determine the peak frequency and bandwidth.

A 100-ns-wide 10-V pulse was delivered to the transducer, with an 80-V_{dc} bias applied. The resulting centerpoint displacement was recorded using LDV. The tests were conducted on the same 100-μm-diameter single element that was tested previously. The result is shown in Fig. 16. By selecting peaks from the impulse response, the damped natural frequency was determined to be 3.0 $\pm$ 0.12 MHz ($N = 3$). Using the log decrement method, the fractional bandwidth is approximately

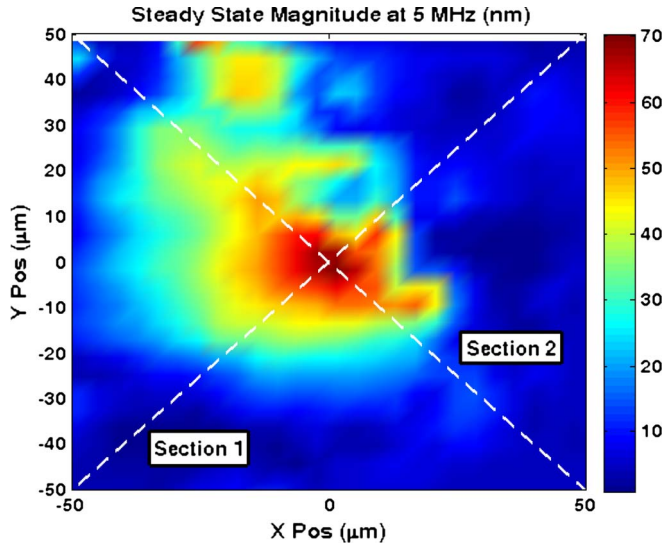

Fig. 17. Two-dimensional laser vibrometry scan of a 100-μm element operating in air while driven with a 9-V_{dc} bias and a 2-V_{ppk} ac drive at 5 MHz. The cross sections along the two diagonals are shown in Fig. 18.

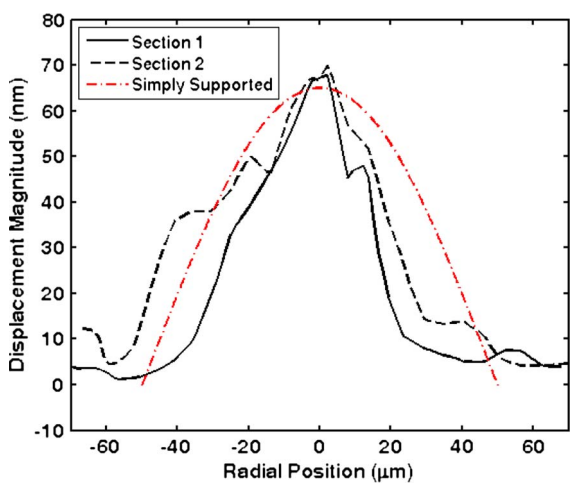

Fig. 18. Measurements of the vibration modeshape of a 100-μm transducer along two different radial cross sections. The location of the two sections is shown in Fig. 17.

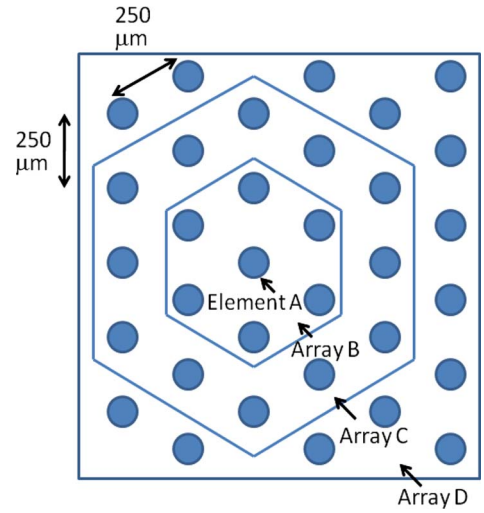

Fig. 19. Configuration of CMUT elements for array testing.

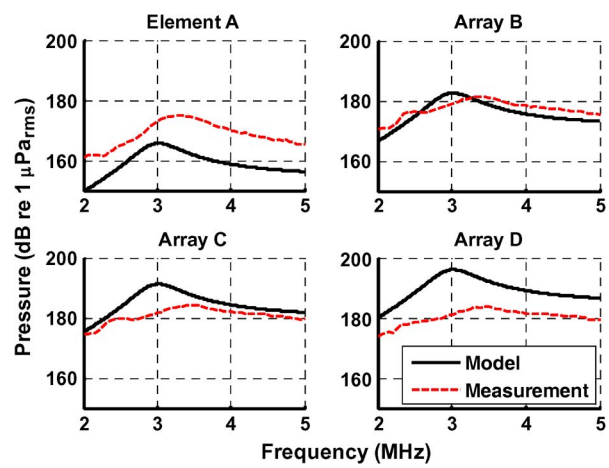

Fig. 20. Computational and experimental results for the on-axis frequency response measured in water at 15 mm from the transducer face with 100-V_{dc} bias plus 100-$V_{peak-to-peak}$ ac drive. Data for a single element and three array configurations are shown. See Fig. 19 for the array layout.

$23\% \pm 4\%$ $(N = 3)$. This is remarkably close to the predicted water-loaded response of the transducer at 2.99 MHz and 21% fractional bandwidth. We expect the model to be a better predictor of bandwidth in water compared to air because the unknown material damping parameters have less influence in the water-loaded case.

Single-point laser vibrometry data have been presented so far in this paper. In all cases, the point of maximum velocity on the surface of the CMUT was measured. Since the transmitted pressure and receive sensitivity for the elements are both directly related to the volume velocity, rather than the single-point velocity, it is important to verify that the ratio between the volume velocity of the transducer and the single-point velocity of the transducer is close to the FEA predicted value of 3.08 10^8 m/m^3. In order to verify this, a 2-D scan of the 100-μm-diameter element was taken in air while driving the element at its resonant frequency of 5 MHz. The magnitude of the observed displacement is shown in Fig. 17. The maximum displacement magnitude for this drive case is 70.1 nm. The total volume displacement was computed by numerically integrating the 2-D scan using a trapezoidal integration rule over the 40 point by 40 point scan and results in a total volume displacement for this drive case of 2.29×10^{-16} m^3. The ratio is 3.06 10^8 m/m^3, which is remarkably close to the FEA predicted value. This justifies the use of the single-point frequency response curves used throughout this paper and indicates that the fractional bandwidth and peak frequencies extracted from these single-point measurements are similar to those seen in the transmitted pressure field.

In addition, the 2-D scan of the surface vibration allows experimental comparison with the simply supported static deflection shape which was used in some of the analytical calculations as justified by the aforementioned FEA results. Although the surface vibration pattern is more complicated than the axisymmetric model, the simply supported shape, shown in Fig. 18, is comparable to the shape observed experimentally. Thus, it appears to be a reasonable choice for limiting the

TABLE III
MODEL PREDICTIONS COMPARED TO EXPERIMENTAL RESULTS

			Measured		Modeled	
Diameter (μm)	DC Bias (V)	Environment	Resonant Frequency (MHz)	Fractional Bandwidth (%)	Resonant Frequency (MHz)	Fractional Bandwidth (%)
100	9	air	5.08	0.6	4.59	0.06
80	9	air	7.62	0.2	6.91	0.04
100	80	air	5.05	0.3	4.58	0.06
100	9	vacuum	5.08	0.6	4.59	0.002
100	80	oil	3.0 ± 0.12	23 ± 4	2.99	21
100	100	water	3.3	28	3.02	22
Array B	100	water	3.5	32	3.02	22
Array C	100	water	3.5	44	3.02	22
Array D	100	water	3.5	44	3.02	22

complexity of the computations while preserving a realistic model.

B. Water-Tank Testing

Water-tank testing has been carried out for arrays of 100-μm-diameter elements. Data were collected using a factory-calibrated 400-μm-diameter hydrophone (Model HGL-0400, Onda Corporation, Sunnyvale, CA) suspended 15 mm in front of the surface of the transmitting array on the array centerline. The hydrophone connects to the oscilloscope through a preamplifier with a calibrated frequency response of 1–20 MHz. The wire bonds and electrical connections to the CMUT array are potted in epoxy to protect them from the water environment. The PECVD oxynitride passivation and sealing layer protects the surface of the CMUT array sufficiently with no additional matching or encapsulation layers. The element or array is biased at 100 V_{dc} and driven with a 100-V peak-to-peak ac burst of 15 cycles at the frequency of interest. The first arrival acoustic response of the hydrophone is recorded, and the peak-to-peak transmitted pressure is extracted from the time domain signal. The excitation frequency is swept to build up the frequency response curve.

The CMUTs are laid out on an interleaved hexagonal grid with edges of 250 μm, as shown in Fig. 19. The array layout is sparse in this test setup to allow room for routing lines and circuits. The sparse layout is expected to reduce the system bandwidth and total pressure output. Much higher array densities are achievable by stacking the CMUTs on the top of the electronic components of the system, which will be done in future work. A single element and three array configurations, shown in the figure, have been tested in transmit mode in the water tank. The results are shown in Fig. 20 and are summarized along with the other testing and modeling results in Table III. For a single element, the peak frequency is 3.3 MHz with a fractional bandwidth of 28%. The model predicts a peak frequency of 3 MHz and a bandwidth of 22%, which is similar to the measured result, considering that no parameters of the model have been tuned in any way.

As the size of the array increases to 7, 19, or 33 elements, the bandwidth increases to 32% and then 44%, and the peak frequency shifts up slightly to 3.5 MHz. This effect is not captured in the uncoupled array model, which does not predict any change in the peak frequency or bandwidth for the on-axis frequency response as the number of elements increases. The source of the increase in bandwidth as the array grows in size is not known. Unmodeled coupling is one possible cause.

The arrays produce on-axis pressures of 181 to 184 dB re 1 μPa_{rms} at the test location. This is identical to the pressure predicted by the model at this test location for Array B. However, for Array C and Array D, the measured pressure is somewhat lower than that predicted by the linear model. The cause of this discrepancy is not known, although unmodeled coupling between elements is suspected.

V. CONCLUSION

A CMUT-in-CMOS device has been described and demonstrated. The transducer elements are fabricated using interconnect and dielectric layers in an n-well CMOS fabrication process. Unlike previous efforts toward integrating CMUTs with CMOS, this process adds no MEMS-related steps to the CMOS process and requires no critical lithography steps after the CMOS process is complete. Only minimal postprocessing is required.

In order to model this device, a method of combining FEA and lumped-element modeling for CMUT elements has been described. An efficient computational strategy has been described, which accounts for the effects of incomplete electrode coverage, nonlinear bias-dependent electrostatic coupling, and environmental loading. Only three finite-element runs are required to determine all the parameters necessary for the computation. The results have shown that the devices respond with a spatial motion that is very similar to the axisymmetric simply supported static bending modeshape. Advantage can be taken from this fact to reduce the computational burden, particularly in regard to computation of the electrostatic coupling parameters.

Computational predictions have been compared to the experimental results obtained via laser vibrometry and water-tank testing. The modeling method is shown to be accurate, predicting the resonant frequency of the transducer designs in oil, in water, in air, and in vacuum within 10% of the experimental values, as well as providing predictions of the fractional

bandwidth that lie within experimental uncertainty for submerged testing of single elements. For in-air and *in vacuo* testing, the model slightly underpredicts the bandwidth due to unmodeled material damping effects which are significant in these regimes. The model predictions are achieved using previously published material property values with no modification or tuning, thus opening a path for future computational optimization work of both individual elements and arrays.

Arrays of 7 to 33 CMUT-in-CMOS elements achieve a center frequency of 3.5 MHz and a fractional bandwidth of 32%–44% when operated in a water tank. The on-axis peak transmitted pressure for the arrays at 15 mm from the transducer face is 181–184 dB re 1 $\mu\mathrm{Pa}_{\mathrm{rms}}$. This paper has focused primarily on the design, fabrication, and modeling of single CMUT-in-CMOS elements. The arrays described in this paper were designed to allow routing lines and circuits to lie between transducer elements, resulting in a sparse fill factor. This is expected to result in a lower fractional bandwidth and a lower transmit pressure than those that can be achieved by densely packed arrays. Dense arrays will be produce in the future by using additional metallization layers in the process to fabricate the transducers and stacking them on the top of the CMOS electronics. This paper has laid the groundwork for the higher density chips by showing the feasibility of using CMOS layers to achieve transducers and developing and validating the needed modeling tools.

ACKNOWLEDGMENT

The authors would like to thank J. Hoffman for his assistance in the Tufts machine shop, V. Miraglia of Tufts Bray Laboratories, M. Doire of Tufts Advanced Technology Laboratory, and L. Polidora and D. Della Pasqua of the Department of Mechanical Engineering, Tufts University.

REFERENCES

[1] T. Ritter, X. C. Geng, K. K. Shung, P. D. Lopath, S. E. Park, and T. R. Shrout, "Single crystal PZN/PT-polymer composites for ultrasound transducer applications," *IEEE Trans. Ultrason., Ferroelectr., Freq. Control*, vol. 47, no. 4, pp. 792–800, Jul. 2000.

[2] K. K. Shung, J. M. Cannata, and Q. F. Zhou, "Piezoelectric materials for high frequency medical imaging applications: A review," *J. Electroceram.*, vol. 19, no. 1, pp. 141–147, Sep. 2007.

[3] C. S. Desilets, J. D. Fraser, and G. S. Kino, "Design of efficient broadband piezoelectric transducers," *IEEE Trans. Sonics Ultrason.*, vol. SU-25, no. 3, pp. 115–125, May 1978.

[4] G. S. Kino, *Acoustic Waves: Devices, Imaging and Analog Signal Processing*. Englewood Cliffs, NJ: Prentice-Hall, 1987, ser. Prentice-Hall signal processing series.

[5] I. Ladabaum, X. Jin, H. T. Soh, A. Atalar, and B. T. Khuri-Yakub, "Surface micromachined capacitive ultrasonic transducers," *IEEE Trans. Ultrason., Ferroelectr., Freq. Control*, vol. 45, no. 3, pp. 678–690, May 1998.

[6] M. I. Haller and B. T. Khuri-Yakub, "A surface micromachined electrostatic ultrasonic air transducer," in *Proc. IEEE Ultrason. Symp.*, 1994, pp. 1241–1244.

[7] P. C. Eccardt, K. Niederer, T. Scheiter, and C. Hierold, "Surface micromachined ultrasound transducers in CMOS technology," in *Proc. IEEE Ultrason. Symp.*, 1996, pp. 959–962.

[8] M. I. Haller and B. T. Khuri-Yakub, "A surface micromachined electrostatic ultrasonic air transducer," *IEEE Trans. Ultrason., Ferroelectr., Freq. Control*, vol. 43, no. 1, pp. 1–6, Jan. 1996.

[9] H. T. Soh, I. Ladabaum, A. Atalar, C. F. Quate, and B. T. Khuri Yakub, "Silicon micromachined ultrasonic immersion transducers," *Appl. Phys. Lett.*, vol. 69, no. 24, pp. 3674–3676, Dec. 1996.

[10] X. Jin, I. Ladabaum, F. L. Degertekin, S. Calmes, and B. T. Khuri-Yakub, "Fabrication and characterization of surface micromachined capacitive ultrasonic immersion transducers," *J. Microelectromech. Syst.*, vol. 8, no. 1, pp. 100–114, Mar. 1999.

[11] O. Ahrens, A. Buhrdorf, D. Hohlfeld, L. Tebje, and J. Binder, "Fabrication of gap-optimized CMUT," *IEEE Trans. Ultrason., Ferroelectr., Freq. Control*, vol. 49, no. 9, pp. 1321–1329, Sep. 2002.

[12] G. Caliano, R. Carotenuto, A. Caronti, and M. Pappalardo, "cMUT echographic probes: Design and fabrication process," in *Proc. IEEE Ultrason. Symp.*, 2002, pp. 1067–1070.

[13] O. Oralkan, A. S. Ergun, J. A. Johnson, M. Karaman, U. Demirci, K. Kaviani, T. H. Lee, and B. T. Khuri-Yakub, "Capacitive micromachined ultrasonic transducers: Next-generation arrays for acoustic imaging?" *IEEE Trans. Ultrason., Ferroelectr., Freq. Control*, vol. 49, no. 11, pp. 1596–1610, Nov. 2002.

[14] B. Bayram, G. G. Yaralioglu, M. Kupnik, A. S. Ergun, O. Oralkan, A. Nikoozadeh, and B. T. Khuri-Yakub, "Dynamic analysis of capacitive micromachined ultrasonic transducers," *IEEE Trans. Ultrason., Ferroelectr., Freq. Control*, vol. 52, no. 12, pp. 2270–2275, Dec. 2005.

[15] C. Leavens, R. Willams, P. Burns, and M. Sherar, "The use of phase codes in ultrasound imaging: SNR gain and bandwidth requirements," *Appl. Acoust.*, vol. 70, no. 10, pp. 1340–1351, Oct. 2009.

[16] N. W. McLachlan, "The stretched membrane electrostatic loudspeaker," *J. Acoust. Soc. Amer.*, vol. 5, no. 2, pp. 167–171, Oct. 1933.

[17] E. C. Wente, "The sensitivity and precision of the electro-static transmitter for measuring sound intensities," *Phys. Rev.*, vol. 19, no. 5, pp. 498–503, May 1922.

[18] J. H. Cantrell and J. S. Heyman, "Electrostatic transducer for absolute measurement of ultrasonic wave displacement amplitude in liquids," *J. Acoust. Soc. Amer.*, vol. 64, no. S1, p. S9, Nov. 1978.

[19] J. H. Cantrell, J. S. Heyman, W. T. Yost, M. A. Torbett, and M. A. Breazeale, "Broad-band electrostatic acoustic transducer for ultrasonic measurements in liquids," *Rev. Sci. Instrum.*, vol. 50, no. 1, pp. 31–33, Jan. 1979.

[20] A. Lohfink and P. C. Eccardt, "Linear and nonlinear equivalent circuit modeling of CMUTs," *IEEE Trans. Ultrason., Ferroelectr., Freq. Control*, vol. 52, no. 12, pp. 2163–2172, Dec. 2005.

[21] G. G. Yaralioglu, S. A. Ergun, and B. T. Khuri-Yakub, "Finite-element analysis of capacitive micromachined ultrasonic transducers," *IEEE Trans. Ultrason., Ferroelectr., Freq. Control*, vol. 52, no. 12, pp. 2185–2198, Dec. 2005.

[22] S. T. Hansen, A. Turo, F. L. Degertekin, and B. T. Khuri-Yakub, "Characterization of capacitive micromachined ultrasonic transducers in air using optical measurements," in *Proc. IEEE Ultrason. Symp.*, 2000, pp. 947–950.

[23] A. S. Ergun, Y. Huang, X. Zhuang, Ö. Oralkan, G. G. Yarahoglu, and B. T. Khuri-Yakub, "Capacitive micromachined ultrasonic transducers: Fabrication technology," *IEEE Trans. Ultrason., Ferroelectr., Freq. Control*, vol. 52, no. 12, pp. 2242–2258, Dec. 2005.

[24] Y. Huang, A. S. Ergun, E. Haeggstrom, M. H. Badi, and B. T. Khuri-Yakub, "Fabricating capacitive micromachined ultrasonic transducers with wafer-bonding technology," *J. Microelectromech. Syst.*, vol. 12, no. 2, pp. 128–137, Apr. 2003.

[25] X. Zhuang, A. S. Ergun, Y. Huang, I. O. Wygant, O. Oralkan, and B. T. Khuri-Yakub, "Integration of trench-isolated through-wafer interconnects with 2D capacitive micromachined ultrasonic transducer arrays," *Sens. Actuators A, Phys.*, vol. 138, no. 1, pp. 221–229, Jul. 2007.

[26] X. Zhuang, I. O. Wygant, D. S. Lin, M. Kupnik, O. Oralkan, and B. T. Khuri-Yakub, "Wafer-bonded 2-D CMUT arrays incorporating through-wafer trench-isolated interconnects with a supporting frame," *IEEE Trans. Ultrason., Ferroelectr., Freq. Control*, vol. 56, no. 1, pp. 182–192, Jan. 2009.

[27] I. O. Wygant, X. Zhuang, D. T. Yeh, O. Oralkan, A. S. Ergun, M. Karaman, and B. T. Khuri-Yakub, "Integration of 2D CMUT arrays with front-end electronics for volumetric ultrasound imaging," *IEEE Trans. Ultrason., Ferroelectr., Freq. Control*, vol. 55, no. 2, pp. 327–342, Feb. 2008.

[28] C. Daft, S. Calmes, D. da Graca, K. Patel, P. Wagner, and I. Ladabaum, "Microfabricated ultrasonic transducers monolithically integrated with high voltage electronics," in *Proc. IEEE Ultrason. Symp.*, 2004, pp. 493–496.

[29] R. A. Noble, A. D. R. Jones, T. J. Robertson, D. A. Hutchins, D. R. Billson, and M. Dera, "Novel, wide bandwidth, micromachined ultrasonic transducers," *IEEE Trans. Ultrason., Ferroelectr., Freq. Control*, vol. 48, no. 6, pp. 1495–1507, Nov. 2001.

[30] L. Beranek, *Acoustics*. New York: AIP, 1986.

[31] L. E. Kinsler, A. R. Frey, A. B. Coppens, and J. V. Sanders, *Fundamentals of Acoustics*. New York: Wiley, 1999.
[32] J. C. Marshall and P. T. Vernier, "Electro-physical technique for post-fabrication measurements of CMOS process layer thicknesses," *J. Res. Nat. Inst. Stand. Technol.*, vol. 112, no. 5, pp. 223–256, Oct. 2007.
[33] J. C. Marshall, D. L. Herman, P. T. Vernier, D. L. DeVoe, and M. Gaitan, "Young's modulus measurements in standard IC CMOS processes using MEMS test structures," *IEEE Electron Device Lett.*, vol. 28, no. 11, pp. 960–963, Nov. 2007.
[34] J. Laconte, D. Flandre, and J. P. Raskin, *Micromachined Thin-Film Sensors for SOI-CMOS Co-Integration*. Dordrecht, The Netherlands: Springer-Verlag, 2006.
[35] M. J. Madou, *Fundamentals of Microfabrication: The Science of Miniaturization*. Boca Raton, FL: CRC Press, 2002.
[36] J. Thurn, R. F. Cook, M. Kamarajugadda, S. P. Bozeman, and L. C. Stearns, "Stress hysteresis and mechanical properties of plasma-enhanced chemical vapor deposited dielectric films," *J. Appl. Phys.*, vol. 95, no. 3, pp. 967–976, Feb. 2004.
[37] X. Cheng, D. F. Lemmerhirt, O. D. Kripfgans, M. Zhang, C. Yang, C. A. Rich, and J. B. Fowlkes, "CMUT-in-CMOS ultrasonic transducer arrays with on-chip electronics," in *Proc. IEEE Int. Conf. Solid-State Sens., Actuators, Microsyst.*, Denver, CO, Jun. 2009, pp. 1222–1225.

Christopher B. Doody (S'07–M'09) received the B.S. degree in mechanical engineering from Worcester Polytechnic Institute, Worcester, MA, in 2007, and the M.S. degree in mechanical engineering from Tufts University, Medford, MA, in 2009. His M.S. thesis focused on the characterization and modeling of capacitive micromachined ultrasound transducers for medical ultrasound purposes through the use of a hybrid finite-element/lumped-element modeling scheme.

From 2007 to 2009, he was a Research Assistant at Tufts University. Since 2009, he has been with STD Med, Inc., Stoughton, MA, where he is currently a Mechanical Design Engineer. His research interests include the design, development, and manufacturing of medical devices in various fields.

Mr. Doody is a member of the American Society of Mechanical Engineers.

Xiaoyang Cheng (S'06–M'09) received the B.S. degree in mechanical engineering from Huazhong University of Science and Technology, Wuhan, China, the M.S. degree from South China University of Technology, Guangzhou, China, and the Ph.D. degree in electrical engineering from The University of New Mexico, Albuquerque, in 2008. His Ph.D. dissertation focused on the development of minimally invasive microelectromechanical systems (MEMS) ultrasound transducers [capacitive micromachined ultrasound transducers (CMUTs)] for biomedical applications.

Since 2008, he has been with Sonetics Ultrasound, Inc., Ann Arbor, MI, where he is currently a Senior Electronics Engineer working on the development of CMUT arrays for medical diagnosis. His research interests include capacitive sensing, MEMS interface circuit design, and CMOS–MEMS integration.

Collin A. Rich (S'95–M'00) received the B.S.E.E. degree from the University of Illinois, Urbana-Champaign, in 1994, and the M.S. and Ph.D. degrees in electrical engineering from the University of Michigan, Ann Arbor, in 1997 and 2000, respectively. His doctoral work focused on thermopneumatically actuated silicon microvalves for microflow control using MEMS fabrication techniques.

His subsequent industrial career has focused on new life-science products using both MEMS and non-MEMS technologies. He was with Integrated Sensing Systems, Inc., Ypsilanti, MI, where he developed patented MEMS-based implantable pressure-sensing devices. He subsequently cofounded Sonetics Ultrasound, Inc., Ann Arbor, the focus of which is MEMS-based 2-D transducer arrays for true 3-D/4-D volumetric ultrasound and where he is currently Chief Technology Officer. In addition, he cofounded Accuri Cytometers, Inc., Ann Arbor, which is leading the development of a market-transforming patented flow cytometer instrument that now enjoys worldwide distribution. He has coauthored several technical publications and is the holder of 14 issued patents as well as multiple pending applications.

David F. Lemmerhirt (S'98–M'05) was born in Aurora, IL, in 1975. He received the B.S.E.E. degree from the University of Illinois, Urbana-Champaign, in 1997, and the M.S. and Ph.D. degrees in electrical engineering from the University of Michigan, Ann Arbor, in 1999 and 2005, respectively.

In 1996, he was a Technical Associate at Lucent Technologies (Bell Labs), Naperville, IL. In 1998, he became a Member of Technical Staff with Intel Corporation, Hillsboro, OR. Since 2004, he has been with Sonetics Ultrasound, Inc., Ann Arbor, where he is currently a Senior Research and Development Engineer. He is the author of multiple technical publications and is the holder of two issued patents and five pending applications. His past research activities include compound semiconductor devices, micromachined sensors and actuators, and multisensor microsystems. He is currently engaged in the development of CMOS-based microelectromechanical systems ultrasound transducer arrays for medical monitoring and imaging.

Dr. Lemmerhirt was a recipient of the College of Engineering Distinguished Achievement Award and the Outstanding Service Award from the National Science Foundation Engineering Research Center for Wireless Integrated MicroSystems at the University of Michigan.

Robert D. White (S'00–M'05) received the B.S. and M.S. degrees in mechanical engineering from the Massachusetts Institute of Technology, Cambridge, in 1999, and the Ph.D. degree in mechanical engineering from the University of Michigan, Ann Arbor, in 2005.

From 1999 to 2000, he was a MEMS Test Engineer at The Charles Stark Draper Laboratories, Cambridge, where he worked on microelectromechanical systems gyroscopes and accelerometers. Since 2005, he has been an Assistant Professor of mechanical engineering at Tufts University, Medford, MA, where he has directed the Tufts Micro and Nano Fabrication Facility since 2007. He teaches in the areas of microsystems, acoustics, dynamics, and controls. He is the author of multiple technical publications and patents. His primary research interests include the design, fabrication, modeling, and testing of acoustic microsystems, with additional work in inner ear mechanics, acoustics and vibrations, and mechatronics.

Prof. White was a recipient of the Charles Stark Draper Laboratory Fellowship in 1998, the National Science Foundation Graduate Research Fellowship in 2001, and the Rackham Predoctoral Fellowship in 2004. He is a member of the Acoustical Society of America, American Society of Mechanical Engineers, and American Institute of Aeronautics and Astronautics.